Flatland wakes based on leaky hyperbolic polaritons

Na Chen[1,2,7], Hanchao Teng[1,2,3,7], Hai Hu[1,2] ✉, Min Liu[1,2], Chengyu Jiang[1,2], Zhuoxin Xue[1,2], Hualong Zhu[1,2], Jiayi Gui[1,2], Peining Li[4], Andrea Alù[5,6] ✉ & Qing Dai[3] ✉

Hyperbolic polaritons facilitate nanoscale light manipulation, but strong field confinement limits their transmission across interfaces. Conversely, leaky waves can convert radiation from confined sources towards the far field. Here we combine hyperbolic polaritons and leaky wave radiation to demonstrate flatland leaky polaritonic wakes. We employ a mixed-dimensional van der Waals heterostructure consisting of a nanoscale waveguide strip on a van der Waals film. The waveguide mode, confined inside the hyperbolic light cone of the background film, enables efficient directional in-plane emission of fast phonon polaritons. The constructive interference of these leaky polaritons generates highly directional polaritonic wakes. Their spatial symmetry can be tailored through the orientation of the heterostructure with respect to the hyperbolic film dispersion. Leveraging van der Waals stacking, we also demonstrate effective acceleration and deceleration of polaritonic wakes by locally tailoring the leaky nano-waveguide dispersion through gradient thickness design. Our findings demonstrate that polaritonic wakes hold promise for integrated nanophotonic circuits.

Polaritons are interface electromagnetic waves generated by the collective oscillations of light coupled to matter excitations, enabling strong field enhancement at the nanoscale[1–5]. Among different families of polaritons, hyperbolic polaritons have garnered notable interest due to their desirable features, such as large optical confinement[6], low damping[7–9] and extreme anisotropy[10–12]. As a result, they have important application prospects in various fields, such as on-chip nanoscale light manipulation[13–21]. However, the extreme field confinement of polaritons limits their propagation across interfaces, impeding the advancement of on-chip photonic devices. In particular, in directions within the plane that are not aligned with the polariton propagation, achieving a long-range connection between polaritonic devices is challenging. Moreover, hyperbolic polaritons are observed only in the very near field of their excitation and undergo severe exponential decay, making energy coupling between different structures more difficult. Limited solutions are available to tackle the issue of polariton interconnects.

In a distinct domain, leaky waves are commonly used to direct electromagnetic radiation towards the far field in preferred directions with high efficiency[22,23]. These waves travel along open guiding structures, gradually releasing their energy into the surrounding medium as they propagate. When their energy is released into radiation, V-shaped trails are formed, akin to the wakes observed by Lord Kelvin behind a

[1]CAS Key Laboratory of Nanophotonic Materials and Devices, CAS Key Laboratory of Standardization and Measurement for Nanotechnology, National Center for Nanoscience and Technology, Beijing, P. R. China. [2]Center of Materials Science and Optoelectronics Engineering, University of Chinese Academy of Sciences, Beijing, P. R. China. [3]School of Materials Science and Engineering, Shanghai Jiao Tong University, Shanghai, P. R. China. [4]Wuhan National Laboratory for Optoelectronics and School of Optical and Electronic Information, Huazhong University of Science and Technology, Wuhan, P. R. China. [5]Photonics Initiative, Advanced Science Research Center, City University of New York, New York, NY, USA. [6]Physics Program, Graduate Center, City University of New York, New York, NY, USA. [7]These authors contributed equally: Na Chen, Hanchao Teng. ✉e-mail: huh@nanoctr.cn; aalu@gc.cuny.edu; daiqing@sjtu.edu.cn

https://doi.org/10.1038/s41563-025-02280-0

moving ship. This phenomenon occurs when the phase velocity of the source exceeds the phase velocity of the leaky waves generated in the medium, resulting in interference fringes that form a polarization trail. This controlled energy release enables beam scanning and shaping, which is advantageous for applications requiring directional radiation, such as communication and radar systems[11,24–28]. While traditional leaky wave structures in the microwave domain are often large, making on-chip integration challenging, their control of far-field connectivity between distant structures offers a promising approach to overcome the challenge of polariton interconnects.

In this study we combine the confinement of polaritons with leaky wave radiation to form flatland wakes based on leaky hyperbolic polaritons. These polaritonic wakes (PWs) can tackle the issue of connecting polariton devices by harnessing radiation leakage to enhance and direct polariton propagation in the plane. Specifically, we achieve this feat by exploiting confined polariton modes in a one-dimensional (1D) nanostrip waveguide residing on a two-dimensional (2D) underlying anisotropic van der Waals (vdW) polaritonic background medium. Fast polaritons leak from the waveguide into the background film within the interface plane, generating line-like leaky waves through interference, analogous to Cherenkov radiation from an electron beam, but in a 2D hyperbolic space. We demonstrate control over the spatial symmetry of the PWs by changing the heterostructure orientation with respect to the crystal axis. Furthermore, by leveraging stackable vdW materials to create non-uniform wedge waveguides, we also demonstrate effective acceleration and deceleration of polaritons in the open nanostrip, enabling the shaping of the wave-front of the PWs and excitation of multi-mode PWs at a single illumination frequency. Our work demonstrates that PWs can combine the nanoscale confinement of polaritons with the directional emission properties of leaky waves, creating a paradigm for efficiently coupling 1D localized modes into 2D flatland near-field optics. This approach provides flexible control over long-range transmission, opening new possibilities for integrated photonic applications.

In-plane anisotropic polaritonic wakes

In general, a functional polaritonic device comprises two key components: a feeding structure or a launcher, which initiates polariton waves, and an underlying dispersive medium that guides and modulates these waves. We leverage tailored polaritonic nano-waveguides to launch and control directional leaky polaritonic waves in layered natural materials, both in in-plane isotropic hexagonal boron nitride (h-BN) and anisotropic α-MoO_3 crystals. The nano-waveguide operates as the flatland 2D analogue of a leaky wave antenna[22].

As illustrated in Fig. 1a–c, a 400-nm-wide strip is excised on an α-MoO_3 film along the crystal axis [100] and subsequently positioned on another uniform α-MoO_3 film to realize a mixed vdW heterostructure with a twisted angle θ of its crystal axis. The isofrequency contours (IFCs) of the hybrid phonon polaritons supported by this mixed heterostructure can be tuned from an open hyperbolic shape to a closed one (also known as a polaritonic topological transition), governed by the twisted angle[29–32] (Supplementary Note 1). The heterostructure forms an open nano-waveguide (Supplementary Figs. 1 and 2) excited by a gold antenna on one end, which supports fast hybrid polaritons longitudinally along the nanostrip. In turn, a portion of the guided energy leaks into the bottom film, yielding flatland polaritonic wakes[23,27] (Fig. 1d). Hyperbolic polariton background films are ideally suited to support flatland leaky waves due to their surface wave dispersion properties.

The underlying mechanism responsible for the emergence of PWs shares similarities with various well-known physical phenomena, including the fluid dynamics of Kelvin wakes and the sonic boom, as well as electromagnetic domains such as Cherenkov and leaky waves[23,27,33–35]. These phenomena occur when the excitation source moves faster than the wave speed in the background medium. The leaky

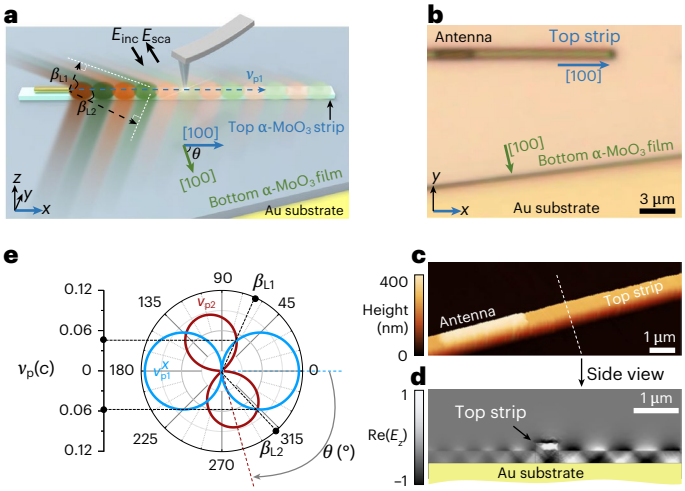

Fig. 1 | Device geometry. a, Schematic of the experimental set-up. A specifically designed α-MoO_3 nanostrip placed on top of an α-MoO_3 film (background) with a twisted angle θ forms a quasi-bound nano-waveguide. A gold antenna on one point of the strip is used to launch hybrid polaritons that propagate longitudinally along the waveguide while simultaneously leaking into the bottom film and inducing PWs. The leaky angle β_L determines the leaky direction of PWs, and the suffixes indicate their propagating direction, with 1 and 2 corresponding to the left and right sides along the propagation direction of the waveguide polaritons, respectively. The arrows represent the crystallographic direction [100] of the top strip (blue) and bottom film (green). v_{p1} indicates the phase velocity of the waveguide polaritons. E_{inc} and E_{sca} indicate the incident and scattered mid-infrared light, respectively. Here, the x axis is intentionally aligned with the [100] direction of the top strip. **b**, Optical image of a typical device. **c**, Zoomed-in view of topography around the antenna region in **b**. **d**, Calculated spatial distribution of the z component of the electric field in the y–z plane (Re(E_z)) for an open waveguide consisting of a top α-MoO_3 strip on the bottom α-MoO_3 film. The strip is w = 400 nm in width and d_1 = 350 nm in thickness, and the thickness of the bottom film is d_2 = 450 nm. The twisted angle is θ = 75° and the frequency is 897 cm^{-1}. Scale bars in **b**–**d** indicate 3, 1 and 1 μm, respectively. **e**, The polar coordinates depict the relationship between phase velocity v_{p1}^x of hybrid polaritons in the waveguide and v_{p2} of hyperbolic polaritons in the bottom film. v_p denotes the phase velocity of polaritons in the waveguide or bottom film, while c, the speed of light, is used here as a normalization unit.

angle β_L is determined by the ratio of phase velocities between waveguide polaritons in the twisted area ($|v_{p1}|$) and hyperbolic phonon polaritons in the background film ($|v_{p2}|$), $\cos\beta_L = \frac{|v_{p2}|}{|v_{p1}|}$, with the requirement $|v_{p1}| > |v_{p2}|$ to generate PWs due to momentum conservation and phase matching[36].

In our structure, the leaky angle β_L can be related to the twisted angle θ through the equation

$$\cos\beta_L = \frac{|R_{xy}v_{p2}^0|}{|v_{p1}^x|}, \quad (1)$$

where $|v_{p1}^x|$ is the projection of the phase velocity on the x axis (longitudinally along the strip) for waveguide polaritons; v_{p2}^0 is the phase velocity for the original hyperbolic polaritons that has not been rotated; and $R_{xy} = \begin{pmatrix} \cos(\theta) & \sin(\theta) \\ -\sin(\theta) & \cos(\theta) \end{pmatrix}$ is a rotation matrix that transforms the phase velocity v_{p2}^0 to the reference frame of the waveguide (details in Supplementary Note 2). In Fig. 1e, we visually depict the relationship between phase velocities v_{p1}^x (blue) and v_{p2} (red) in polar coordinates. Due to the polariton phase velocity being in-plane anisotropic for the biaxial crystal of α-MoO_3 (Supplementary Fig. 3), the twisted structure breaks in-plane mirror symmetry (from the S_4 to the C_2 group), yielding an asymmetry in leaky angle between the left and right directions.

https://doi.org/10.1038/s41563-025-02280-0

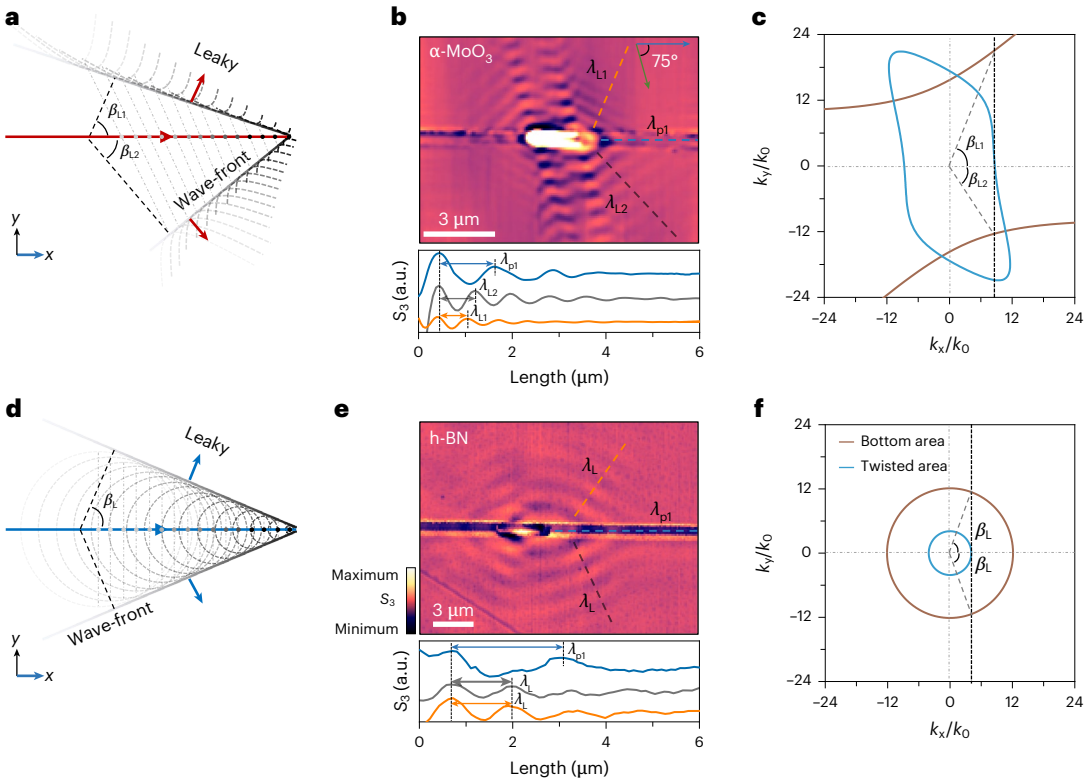

Fig. 2 | Nanoimaging of anisotropic and isotropic PWs. a, Sketch of PWs produced through an envelope of the hyperbolic wave leaked at successive times. **b**, Top: real-space mapping of anisotropic PWs by nanoimaging with s-SNOM. The main parameters of the sample being measured have been depicted in Fig. 1. Bottom: near-field amplitude (S_3) profiles of different modes along the direction represented by dashed lines in the top panel. **c**, IFCs of polaritons in the bottom and twisted areas. The vertical dashed line represents the momentum of the waveguide polaritons in the twisted area. k_x and k_y are the polariton momenta along the x and y directions, while k_0 is the momentum of the incident light in free space. Due to the limitation of the waveguide in the y direction, the waveguide polaritons can propagate only along the x direction, corresponding to IFCs of twisted area with $k_y = 0$. The detailed calculations are depicted in Supplementary Note 3 and Supplementary Fig. 4. **d**, Sketch of isotropic PWs in the h-BN structure. **e**, Real-space nanoimaging of isotropic PWs (top) and corresponding near-field amplitude (S_3) profiles (bottom). The strip is $w = 400$ nm in width and $d_1 = 145$ nm in thickness, and the thickness of the bottom film is $d_2 = 74$ nm. The illumination frequency is 1,400 cm^{-1}. **f**, IFCs of polaritons in the bottom and waveguide areas. The circular in-plane dispersion produces symmetric leaky angle β_L and wave-fronts. The λ_{p1} denotes the waveguide polaritons in the nanostrip, and λ_L, λ_{L1} and λ_{L2} represent the PWs in the left and right sides along the propagation direction of the waveguide polaritons, respectively. Scale bars in **b** and **e** are 3 μm.

Experimental observation of polaritonic wakes

We experimentally observed PWs in our vdW heterostructures by infrared nanoimaging via scattering-type scanning near-field optical microscopy (s-SNOM). A p-polarized laser beam impinges at an angle of 60° relative to the tip axis, illuminating (via electric field E_{inc}) a gold antenna. It launches hybrid polaritons propagating along the nanoscale waveguide (Methods for further details)[37]. We start with a sample of twisted angle $\theta = 75°$ (Fig. 2a–c), for which leaky polaritons can be simultaneously excited in both the left and right directions while showcasing a characteristic asymmetry with moderate propagation losses.

Figure 2a illustrates the interference of leaky hyperbolic waves when the waveguide polariton resides within the light cone of the background film; that is, it lives within the light cone. This interference generates a coherent wave-front that is radiated at a specific leaky angle in the bottom film. In this context, the waveguide polaritons play the role of a travelling-wave excitation source. The top panel of Fig. 2b presents the PWs directly visualized in our real-space imaging experiments. The line-like features (denoted by the wavelengths λ_{L1} and λ_{L2}) reveal the PWs arising from the interference of hyperbolic fast wave[38]. Additionally, our scanning image reveals the waveguide polaritons in the nanostrip (indicated by the wavelength λ_{p1}) and the normal hyperbolic polaritons in the α-MoO_3 bottom film. The twisted angle between the top strip and bottom film triggers an in-plane broken symmetry so that the leaky angles and wavelength of PWs on the left and right sides of the waveguide are different (the bottom panel of Fig. 2b). Notably, the calculated dispersion of the hybrid polariton modes in the twisted region showcases momentum matching that of the leaky PWs[28,39] (Fig. 2c).

For a better understanding of PWs in anisotropic materials, we also consider the in-plane isotropic scenario, studying a similar geometry in h-BN (Fig. 2d–f and Supplementary Fig. 5), for which the IFCs are circular. Again, the waveguide polaritons are prone to leak into the background as flatland leaky modes but through the interference of circular rather than hyperbolic waves. In an in-plane isotropic h-BN medium, the leaky angle is symmetric in both the left and right directions, and it can be simplified as $\beta_L = \arccos(\frac{v_{p2}}{v_{p1}}) = \arccos(\frac{d_1}{d_1+d_2})$, where β_L is dependent solely on the thickness of top h-BN strip (d_1) and bottom h-BN film (d_2) and remains independent of the illumination frequency or dielectric environment. The extracted near-field curves can further confirm the symmetry of the leakage. As depicted in Fig. 2e, it is clear that the leaky angles, wavelengths, amplitudes and phases of the PWs are nearly identical in the h-BN case. This stands in sharp contrast to the anisotropic leakage observed in α-MoO_3.

In our experiments, although the polaritons remain confined within the plane, they propagate as plane waves towards the far field in a flatland geometry. Practical material losses limit their propagation,

https://doi.org/10.1038/s41563-025-02280-0

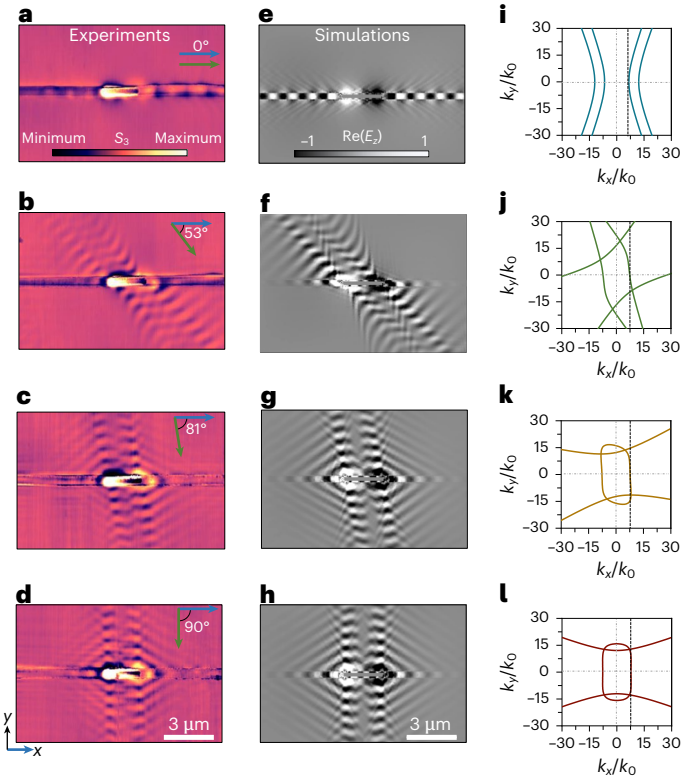

Fig. 3 | Steering PWs by crystal orientation of the heterostructure. a–d, Real-space infrared nanoimages reveal the steering for PWs with $\theta = 0°$ (**a**), 53° (**b**), 81° (**c**) and 90° (**d**). The strip is $w = 400$ nm in width and $d_1 = 240$ nm in thickness, and the thickness of the bottom film is $d_2 = 267$ nm. The illumination frequency is fixed at 897 cm^{-1}. **e–h**, Calculated near-field distribution (real part of the out-of-plane component of the electric field, Re(E_z)) of PWs at different twisted angles corresponding to experimental observations in **a–d**. Scale bars indicate 3 μm in **a–h**. **i–l**, Calculated IFCs of polaritons in the bottom film and waveguide area for different twisted angles of 0° (**i**), 53° (**j**), 81° (**k**) and 90° (**l**). The vertical dashed lines represent the momentum of the waveguide mode in the nanostrip. The IFCs are colour-coded to indicate data from structures with different twisted angles.

but they do not experience the usual cylindrical decay expected due to confined launchers. Thus, our work operates within the framework of '2D far-field' propagation, where leakage occurs from a 1D mode into the 2D flatland. This is analogous to traditional leaky wave antennas, which radiate 1D or 2D fields into three-dimensional (3D) space. Consequently, our PWs bridge the gap between the confinement of 1D polaritons and leaky radiation within the 2D plane.

Manipulating PWs through crystal orientation

Figure 3a–d and Supplementary Figs. 6 and 7 show measured near-field amplitude images of polaritons and the topography of the sample, with twisted angles $\theta = 0°$, 53°, 66°, 74°, 81° and 90°, respectively. The corresponding numerically simulated field distributions are shown in Fig. 3e–h.

At $\theta = 0°$, that is, with the strip oriented along the [100] direction of the bottom α-MoO_3 film, we observe only canalized modes propagating in the waveguide, with barely any fringe found in the bottom film (Fig. 3a). This is due to the nearly parallel hyperbolic IFC of polaritons in the twisted area and bottom film (that is, no intersection exists between the outer hyperbolic IFC of the bottom film and vertical dashed lines (Fig. 3i)), resulting in no momentum matching, which indicates the threshold of the phase velocity.

When θ is increased to 53°, we find only left or right PWs along the nanostrip (Fig. 3b), as the asymmetric IFC supports large mismatching of the wave vector on the other two sides. Further increasing θ can reduce the degree of wave vector mismatching and form PWs on both sides (Fig. 3c), but the modes on the left and right sides are still inconsistent.

In particular, at $\theta = 90°$, we achieve an ideal scenario with no minimum velocity requirement to achieve PWs (Fig. 3d). This effect is typically generated by periodic gratings to form hyperbolic IFCs of the wave medium. Given that α-MoO_3 is an excellent biaxial hyperbolic natural material, it can be regarded as an atomic-scale periodic grating. The in-plane anisotropy of this hyperbolic material leads to a variable velocity threshold that is dependent on the incident angle.

The in-plane structural symmetry substantially enhances the tunability of leaky modes. The evolution of IFCs with varying twist angles influences the excitation threshold, with the symmetry of leaky modes shifting from symmetric to unidirectional and eventually ceasing. Indeed, the leaky angle can be dramatically controlled by rotating the top strip, with β_{L1} between ~60° and 90° for the left PWs, and β_{L2} between 55° and 73° for the right PWs (Supplementary Fig. 8a). Our near-field observations, numerical simulations and theoretical calculations agree well with each other.

We have also conducted a comprehensive investigation of the wavelength and loss of PWs as a function of geometry and frequency. The wavelength of the interference line-like polaritons in the underlying α-MoO_3 film, excited by the hybrid polaritons in the twisted nanostrip, is shorter than that of the hybrid polaritons themselves. Furthermore, their wavelength can be further substantially reduced under an extreme-asymmetry structure configuration (Supplementary Fig. 8b). The damping of PWs is influenced by both the inherent loss of the α-MoO_3 film and an additional decay factor introduced by the waveguide (Supplementary Note 4 and Supplementary Fig. 9). Supplementary Figs. 10 and 11 show PWs in another sample with a thinner α-MoO_3 strip under different illumination frequencies.

Non-uniform PWs by gradient waveguide

Since phonon polaritons are primarily volume modes, their mode confinement is inversely related to the material thickness. This phenomenon is demonstrated by an increase in wavelength and phase velocity as the material thickness grows (Supplementary Fig. 3). The manipulation of phase velocity through material thickness can then be effectively combined with the 2D properties of α-MoO_3, which enables the fabrication of vdW heterostructures with precise gradient height. This approach allows for the generation of locally encoded phase velocities, providing a unique platform for accelerating or decelerating PWs (Fig. 4a–d).

The most critical hurdle in experimentally realizing the acceleration and deceleration of PWs lies in fabricating such structures with precise gradient height. To address this, we explored two fabrication approaches (Supplementary Figs. 14–17 for more details): a bottom-up approach, where we stack multiple α-MoO_3 thin films using a layer-by-layer transfer method to create a stepped slab structure; and a top-down approach, which involves selecting naturally exfoliated α-MoO_3 flakes with gradual slopes and further refining them using a focused ion beam. Using these methods, we successfully fabricated nanostrip waveguides with gradient edges ranging from 350 nm to 20 nm in thickness, featuring a linear slope that either increases or decreases gradually (Fig. 4e–h). This engineered structure allows the propagation of hybridized polaritons with uniformly increasing or decreasing velocities within the nano-waveguide. For 2D materials, these fabrication steps can be performed with atomic-level precision, enabling continuous acceleration and deceleration of the polaritonic waves.

When the waveguide mode propagates with acceleration, the velocity at each location is smaller than the velocity at the following locations (Fig. 4a). As a result, the leaky angle at a given location is smaller than at one of the subsequent regions. Under this continuous evolution, the observed interference of PWs no longer exhibits a

https://doi.org/10.1038/s41563-025-02280-0

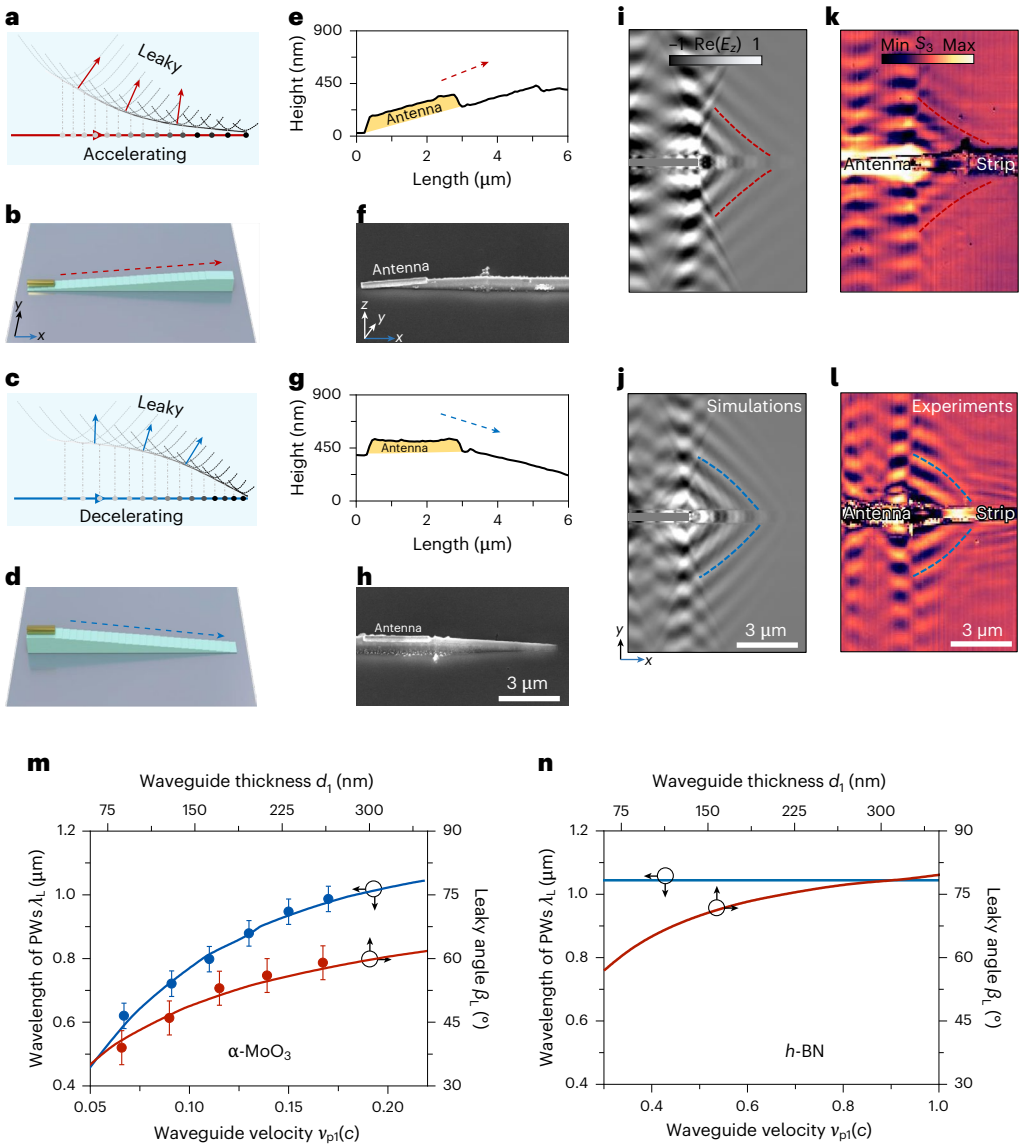

Fig. 4 | Accelerating and decelerating PWs in non-uniform waveguides. **a**,**c**, Diagrammatic sketch of multi-mode PWs produced through an envelope of the hyperbolic polaritons leaked at successive times. The accelerating (**a**) or decelerating (**c**) leaking different hyperbolic polaritons interact in their propagation direction, producing concave wave-front (**a**) and convex wave-front (**c**) propagating at a gradient leaky angle in the bottom film. We considered the case of twisted angle $\theta = 90°$ and show only the left side. **b**,**d**, Three-dimensional illustration of multilayer vdW stacking of the top nanostrips, enabling the construction of non-uniform waveguides in a wedge shape. The arrows indicate an increase (**b**) and decrease (**d**) in the number of layers of nanostrips. **e**–**h**, Scanning electron microscopy (SEM) images (**f** and **h**) and height profiles (**e** and **g**) of two PW devices for accelerating (**e** and **f**) and decelerating (**g** and **h**) PWs in non-uniform waveguides with precise gradient height. The non-uniform regions of the waveguides have a length of 5 μm along the x direction and a varying thickness from 350 nm to 20 nm. The thickness of the bottom α-MoO_3 film is $d_2 = 310$ nm, and the illumination frequency is fixed at 890 cm^{-1}. **i**,**j**, Calculated near-field distributions of curved PWs for the accelerating scenario (concave wave-front; **i**) and decelerating scenario (convex wave-front; **j**). **k**,**l**, Real-space infrared nanoimages of curved PWs for the accelerating (**k**) and decelerating (**l**) scenarios. Note that the parallel fringes at the end of the decelerating devices in **l** are the tip-excited and edge-excited polariton fringes. The dashed curves in **i**–**l** trace the signal maxima (Supplementary Note 5 and Supplementary Fig. 12 for more details). Min, minimum; Max, maximum. **m**,**n**, Theoretically calculated leaky angle β_L and wavelength of PWs as a function of the waveguide thickness d_1 and phase velocity v_{p1} of the hybrid polariton in the α-MoO_3 (**m**) and h-BN (**n**) waveguides. The solid dots in **m** indicate the experimentally retrieved data from **k** and **l** (Supplementary Fig. 13 for more details). Considering the visual estimation errors during data extraction, we take conservative errors of ±4° for the leaky angle β_L and ±40 nm for the wavelength of PWs λ_L. The black arrows on the data indicate the corresponding coordinate axis.

line-like wave-front but instead forms a concave shape (Fig. 4i,k). Conversely, as the thickness of the waveguide gradually decreases, the PWs undergo deceleration, causing the leaky angle to decrease gradually along the propagation direction of the waveguide polaritons (Fig. 4c). Consequently, we observe a leaked convex wave-front of PWs (Fig. 4j,l, Supplementary Note 5 and Supplementary Fig. 12). The variation in acceleration and deceleration of waveguide polaritons results in different wavelengths for PWs at varying leaky angles (Supplementary Fig. 13). Thus, in this configuration, we can generate polaritons with multiple wavelengths in the bottom α-MoO_3 layer by the non-uniform waveguide under incident light at only a single frequency. This approach appears to offer benefits in terms of integration of on-chip excitation.

Figure 4m,n shows a comprehensive analysis and comparison of the relationship between the material thickness of the top strip and the velocity of the waveguide mode, in relation to the wavelength

and leaky angle of the PWs. Increasing the thickness of the top strip increases the phase velocity of the waveguide polaritons, leading to a narrower cone of PWs. This causes the leaky angle to increase from 32° to 62°, along with an increase in the leaky wavelength from 460 nm to 1,140 nm (Fig. 4m). As hyperbolic polaritons propagate, diffraction continuously alters their wave-front shape. This results in slight variations in leaky wave angles at different spatial positions. To simplify our analysis, we focused our analysis on a single fringe with relatively higher amplitude and larger wave-front size, marked by the red and blue dashed curves in Fig. 4i–l.

By contrast, the acceleration and deceleration of polaritons in the h-BN waveguide only induce changes in the leaky angle from 56° to 81°, without causing any alteration in the wavelength of PWs, due to the in-plane isotropy characteristics (Fig. 4n). As shown in Supplementary Fig. 18, we also performed experimental measurements on three devices with different nanostrip thicknesses and extracted the leaky wave angles and wavelengths. These results from discrete devices not only validate the thickness-dependent tunability of leaky modes but also provide additional corroboration for our experimental conclusions regarding acceleration and deceleration.

Note that the excitation of such PWs by moving electrons would require the acceleration of electron energy on the order of thousands of electronvolts, usually by means of nuclear reactions or static high voltages. By contrast, our scheme relies on the leakage of phonon polaritons, requiring only ~0.1 eV of incident photons, reducing the required energy by four orders of magnitude. This stems from the fact that the mass of the polariton as a quasiparticle is much lower than the effective mass of an electron or other charged particle[40]. In addition, our structure is less susceptible to illumination polarization compared with metal nanowires as a launching source[41,42].

In conclusion, we introduced PWs as a powerful approach for efficiently exciting and directionally emitting nanoscale polaritons. Our approach relies on a mixed-dimensional nano-waveguide that generalizes traditional leaky waves to hyperbolic planar interfaces, enabling directional emission of fast phonon polaritons. These fast polaritons leak from the waveguide into the background film along the interface plane, producing line-like leaky waves through interference. This phenomenon is analogous to Cherenkov radiation emitted by an electron beam, but it occurs within a 2D hyperbolic space. Furthermore, the wavelength and leaky angle of the PWs can be tailored through the waveguide thickness and spatial symmetry engineering in the case of an anisotropic background. Leveraging vdW stacking, we also demonstrated effective acceleration or deceleration of these hybrid polaritons. This, in turn, enables PWs with curved wave-fronts, offering notable advantages in terms of integration for on-chip communications based on polaritons. Our PWs may serve as a bridge, connecting the confinement of 1D polaritons to leaky radiation in the 2D plane. This 1D-to-2D coupling approach can be viewed as an extension of and complement to the traditional 3D far-field optical coupling to the 2D near field while providing multidimensional control over the direction, wavelength and beam shaping of nanoscale polaritons.

Future research presents several promising avenues. For instance, integrating graphene heterostructures could lead to the development of electrically tunable and switchable leaky modes[10,43–46]. Exploring polariton leakage in the temporal domain offers opportunities to investigate interactions and non-equilibrium effects, such as the Doppler effect[47] and hydrodynamic wakes[48,49]. Additionally, introducing various material systems to adjust the directional relationship between the phase and group velocities of polaritons can enhance energy manipulation. These advancements are poised to greatly impact the development of sophisticated polaritonic nanodevices and on-chip circuits.

Online content

Any methods, additional references, Nature Portfolio reporting summaries, source data, extended data, supplementary information, acknowledgements, peer review information; details of author contributions and competing interests; and statements of data and code availability are available at https://doi.org/10.1038/s41563-025-02280-0.

References

1. Zhang, Q. et al. Interface nano-optics with van der Waals polaritons. *Nature* **597**, 187–195 (2021).
2. Wu, Y. et al. Manipulating polaritons at the extreme scale in van der Waals materials. *Nat. Rev. Phys.* **4**, 578–594 (2022).
3. Guo, X. et al. Polaritons in van der Waals heterostructures. *Adv. Mater.* **35**, 2201856 (2022).
4. Hu, H. et al. Far-field nanoscale infrared spectroscopy of vibrational fingerprints of molecules with graphene plasmons. *Nat. Commun.* **7**, 12334 (2016).
5. Hu, H. et al. Gas identification with graphene plasmons. *Nat. Commun.* **10**, 1131 (2019).
6. Dai, S. et al. Tunable phonon polaritons in atomically thin van der Waals crystals of boron nitride. *Science* **343**, 1125–1129 (2014).
7. Ma, W. et al. In-plane anisotropic and ultra-low-loss polaritons in a natural van der Waals crystal. *Nature* **562**, 557–562 (2018).
8. Taboada-Gutiérrez, J. et al. Broad spectral tuning of ultra-low-loss polaritons in a van der Waals crystal by intercalation. *Nat. Mater.* **19**, 964–968 (2020).
9. Zheng, Z. et al. A mid-infrared biaxial hyperbolic van der Waals crystal. *Sci. Adv.* **5**, eaav8690 (2019).
10. Wang, C. et al. Van der Waals thin films of WTe_2 for natural hyperbolic plasmonic surfaces. *Nat. Commun.* **11**, 1158 (2020).
11. Ni, X. et al. Observation of directional leaky polaritons at anisotropic crystal interfaces. *Nat. Commun.* **14**, 2845 (2023).
12. Teng, H. et al. Steering and cloaking of hyperbolic polaritons at deep-subwavelength scales. *Nat. Commun.* **15**, 4463 (2024).
13. Ma, W. et al. Ghost hyperbolic surface polaritons in bulk anisotropic crystals. *Nature* **596**, 362–366 (2021).
14. Passler, N. C. et al. Hyperbolic shear polaritons in low-symmetry crystals. *Nature* **602**, 595–600 (2022).
15. Hu, G. et al. Real-space nanoimaging of hyperbolic shear polaritons in a monoclinic crystal. *Nat. Nanotechnol.* **18**, 64–70 (2023).
16. Hu, H. et al. Gate-tunable negative refraction of mid-infrared polaritons. *Science* **379**, 558–561 (2023).
17. Sternbach, A. et al. Negative refraction in hyperbolic hetero-bicrystals. *Science* **379**, 555–557 (2023).
18. Álvarez-Pérez, G. et al. Negative reflection of nanoscale-confined polaritons in a low-loss natural medium. *Sci. Adv.* **8**, eabp8486 (2022).
19. Zhang, T., Zheng, C., Chen, Z. N. & Qiu, C. W. Negative reflection and negative refraction in biaxial van der Waals materials. *Nano Lett.* **22**, 5607–5614 (2022).
20. Duan, J. et al. Planar refraction and lensing of highly confined polaritons in anisotropic media. *Nat. Commun.* **12**, 4325 (2021).
21. Zhang, Q. et al. Unidirectionally excited phonon polaritons in high-symmetry orthorhombic crystals. *Sci. Adv.* **8**, eabn9774 (2022).
22. Moccia, M., Castaldi, G., Alù, A. & Galdi, V. Leaky waves in flatland. *Adv. Opt. Mater.* **12**, 2203121 (2024).
23. Monticone, F. & Alu, A. Leaky-wave theory, techniques, and applications: from microwaves to visible frequencies. *Proc. IEEE* **103**, 793–821 (2015).
24. Karl, N. J., McKinney, R. W., Monnai, Y., Mendis, R. & Mittleman, D. M. Frequency-division multiplexing in the terahertz range using a leaky-wave antenna. *Nat. Photon.* **9**, 717–720 (2015).
25. Matsumoto, H., Watanabe, I., Kasamatsu, A. & Monnai, Y. Integrated terahertz radar based on leaky-wave coherence tomography. *Nat. Electron.* **3**, 122–129 (2020).

26. Huang, H. et al. Leaky-wave metasurfaces for integrated photonics. *Nat. Nanotechnol.* **18**, 580–588 (2023).
27. Kong, G. S., Ma, H. F., Cai, B. G. & Cui, T. J. Continuous leaky-wave scanning using periodically modulated spoof plasmonic waveguide. *Sci. Rep.* **6**, 29600 (2016).
28. Alù, A., Bilotti, F., Engheta, N. & Vegni, L. Subwavelength planar leaky-wave components with metamaterial bilayers. *IEEE Trans. Antennas Propag.* **55**, 882–891 (2007).
29. Hu, G. et al. Topological polaritons and photonic magic angles in twisted α-MoO_3 bilayers. *Nature* **582**, 209–213 (2020).
30. Chen, M. et al. Configurable phonon polaritons in twisted α-MoO_3. *Nat. Mater.* **19**, 1307–1311 (2020).
31. Duan, J. et al. Twisted nano-optics: manipulating light at the nanoscale with twisted phonon polaritonic slabs. *Nano Lett.* **20**, 5323–5329 (2020).
32. Zheng, Z. et al. Phonon polaritons in twisted double-layers of hyperbolic van der Waals crystals. *Nano Lett.* **20**, 5301–5308 (2020).
33. Liu, F. et al. Integrated Cherenkov radiation emitter eliminating the electron velocity threshold. *Nat. Photon.* **11**, 289–292 (2017).
34. Lin, X. et al. Controlling Cherenkov angles with resonance transition radiation. *Nat. Phys.* **14**, 816–821 (2018).
35. Xue, S., Zeng, Y., Bao, Q., Zhu, S. & Chen, H. Tunable Cherenkov radiation based on a van der Waals semiconductor α-MoO_3 and graphene hybrid. *Opt. Lett.* **47**, 2458–2461 (2022).
36. Hu, H. et al. Surface Dyakonov–Cherenkov radiation. *eLight* **2**, 2 (2022).
37. Pons-Valencia, P. et al. Launching of hyperbolic phonon-polaritons in h-BN slabs by resonant metal plasmonic antennas. *Nat. Commun.* **10**, 3242 (2019).
38. Maciel-Escudero, C., Konečná, A., Hillenbrand, R. & Aizpurua, J. Probing and steering bulk and surface phonon polaritons in uniaxial materials using fast electrons: hexagonal boron nitride. *Phys. Rev. B* **102**, 115431 (2020).
39. Moccia, M., Castaldi, G., Alù, A. & Galdi, V. Exploring interface effects in flatland optics. In *2023 Seventeenth International Congress on Artificial Materials for Novel Wave Phenomena (Metamaterials)* X-114–X-116 (IEEE, 2023).
40. Sun, Y. et al. Direct measurement of polariton–polariton interaction strength. *Nat. Phys.* **13**, 870–875 (2017).
41. Zhang, Y. et al. Tunable Cherenkov radiation of phonon polaritons in silver nanowire/hexagonal boron nitride heterostructures. *Nano Lett.* **20**, 2770–2777 (2020).
42. Guo, X. et al. Mid-infrared analogue polaritonic reversed Cherenkov radiation in natural anisotropic crystals. *Nat. Commun.* **14**, 2532 (2023).
43. Hu, H. et al. Doping-driven topological polaritons in graphene/α-MoO_3 heterostructures. *Nat. Nanotechnol.* **17**, 940–946 (2022).
44. Ruta, F. L. et al. Surface plasmons induce topological transition in graphene/α-MoO_3 heterostructures. *Nat. Commun.* **13**, 3719 (2022).
45. Hu, H. et al. Active control of micrometer plasmon propagation in suspended graphene. *Nat. Commun.* **13**, 1465 (2022).
46. Qu, Y. et al. Tunable planar focusing based on hyperbolic phonon polaritons in α-MoO_3. *Adv. Mater.* **34**, 2105590 (2022).
47. Correas-Serrano, D. & Gomez-Diaz, J. S. Nonreciprocal and collimated surface plasmons in drift-biased graphene metasurfaces. *Phys. Rev. B* **100**, 081410 (2019).
48. Rus, J., Bossart, A., Apffel, B., Malléjac, M. & Fleury, R. Experimental observation of parabolic wakes in thin plates. *Phys. Rev. Res.* **6**, L032027 (2024).
49. Chaves, A. J., Peres, N. M. R., Smirnov, G. & Mortensen, N. A. Hydrodynamic model approach to the formation of plasmonic wakes in graphene. *Phys. Rev. B* **96**, 195438 (2017).

Methods

Sample preparation

Supplementary Fig. 19 shows the flow chart of the main sample preparation process. The α-MoO_3 bulk crystals (Shanghai Onway Technology) were mechanically exfoliated onto a SiO_2 (300 nm)/Si (500 μm) substrate and then inspected via optical microscopy and s-SNOM to find suitable α-MoO_3 flakes.

The strips (25 μm × 400 nm) were patterned on α-MoO_3 using 100 kV electron-beam lithography (Vistec EBPG 5000plus ES) on ~1 μm thickness of 950K-molecular weight polymethyl methacrylate (PMMA) lithography resist and then were etched with SF_6 and Ar using reactive ion etching (SENTECH 500 ICP-RIE Plasma Etch System). After that, the sample was immersed in 80 °C acetone for 20 min and isopropyl alcohol (IPA) for 3 min to remove the PMMA, followed by nitrogen gas drying.

The twisted α-MoO_3 sample was prepared through a deterministic dry-transfer process. The bottom α-MoO_3 flake was first transferred onto a gold (60 nm)/Si (500 μm) substrate. Then the as-prepared α-MoO_3 strip was transferred above the bottom α-MoO_3 flake and rotationally aligned to the crystal axes by using a rotation stage under optical microscopy. We demonstrate control over the acceleration and deceleration of PWs using gradient-height structures, fabricated through two approaches. The bottom-up method constructs stepped slabs by sequentially transferring thin films of α-MoO_3, while the top-down approach selects naturally exfoliated α-MoO_3 flakes and refines them with focused ion beam technology (Supplementary Figs. 14–17 for more details).

A gold antenna was fabricated on the α-MoO_3 strip by using 100 kV electron-beam lithography on approximately 350 nm of 950K-molecular weight PMMA lithography resist. Then a 50 nm thickness of Au was deposited by electron-beam evaporation in a vacuum chamber under a pressure of 5×10^{-6} torr. To remove any residual organic materials, the samples were immersed in a hot acetone bath at 80 °C for 25 min and subjected to a gentle rinse of IPA for 3 min, followed by gas drying and thermal baking.

Scanning near-field optical microscopy measurements

We use a commercially available s-SNOM set-up manufactured by Neaspec for performing near-field infrared nanoimaging. A Pt-coated atomic force microscopy tip with a radius of ~25 nm (NanoWorld) was employed, with a tapping frequency and amplitude of ~270 kHz and ~30–50 nm, respectively. The tip is illuminated by a *p*-polarized mid-infrared light from a tunable quantum cascade laser (890–2,000 cm^{-1}). The pseudo-heterodyne interferometer method was used to record the tip-scattered light and demodulate it at the third harmonic (S_3) to effectively suppress background signals.

Extraction of the wave-front curve and leaky angle

We obtained curved lines corresponding to the maximum signal of the curved wave-front in accelerating and decelerating devices by rasterizing the experimental near-field images and sequentially extracting and connecting the pixels with the strongest amplitude, as indicated by the dashed curves in Fig. 4i–l. We then calculated the tangent and normal of these curves. The intersection of the normal with the waveguide represents the waveguide thickness, and the angle between the normal and the *x* axis represents the leaky angle (Supplementary Note 5 and Supplementary Figs. 12 and 13 for more details).

Data availability

The data that support the findings of this study are available within the paper and the Supplementary Information. Source data are provided with this paper.

Acknowledgements

We acknowledge X. Xi and X. Wang (State Key Laboratory of New Ceramics & Fine Processing, Tsinghua University) for scanning near-field optical microscopy measurements and valuable discussions, and are grateful to X. Li (Institutional Center for Shared Technologies and Facilities of Institute of Process Engineering, Chinese Academy of Sciences) for assistance with structural fabrication and characterization. Q.D., H.H. and their team were supported by the National Key Research and Development Program of China (grant no. 2021YFA1201500 to Q.D.), the National Natural Science Foundation of China (grant nos. 52322209, 52172139 and 52350314 to H.H.; grant no. 51925203 to Q.D.), Beijing Nova Program (grant nos. 2022012 and 20240484600 to H.H.) and the Youth Innovation Promotion Association of the Chinese Academy of Sciences (grant no. 2022037 to H.H.). N.C. was supported by the Postdoctoral Fellowship Program and China Postdoctoral Science Foundation (grant nos. BX20250181 and 2024M760685). A.A. was supported by the Office of Naval Research (grant no. N00014-2212448), the Air Force Office of Scientific Research and the Simons Foundation.

Author contributions

Q.D. and H.H. conceived the idea. Q.D. and A.A. supervised the project. N.C. and H.H. led the experiments, prepared the samples and performed the near-field measurements. H.T. and A.A. developed the theory and performed the simulation. N.C., H.T. and H.H. analysed the data, and all authors discussed the results. M.L., C.J., Z.X., H.Z. and J.G. provided experimental and simulation assistance. H.H., N.C., H.T. and Q.D. cowrote the paper, with input and comments from all other authors.

Competing interests

The authors declare no competing interests.

Additional information

Supplementary information The online version contains supplementary material available at https://doi.org/10.1038/s41563-025-02280-0.

Correspondence and requests for materials should be addressed to Hai Hu, Andrea Alù or Qing Dai.

Peer review information *Nature Materials* thanks the anonymous reviewers for their contribution to the peer review of this work.